1. CLIMATE AND ENVIRONMENTAL MODELLING

1.1 Composite Forecast of Rainfall Pattern

Simulation of the observed spatio-temporal structures of tropical precipitation is crucial for prediction of climate and weather. Successful forecasting of rainfall patterns at various spatio-temporal scales can provide significant help in various sectors like agriculture and power generation through long-term planning. However, this continues to be a major scientific challenge; while dynamical models are capable of generating most comprehensive forecasts, most atmospheric general circulation models can claim only moderate skill in forecasting of rainfall patterns. Statistical models, such as power regression model, on the other hand, have been used with some success to generate seasonal forecasts of all-India summer monsoon rainfall (ISMR). However, there is a definite and a strongly-felt need for a better methodology for good quality long-range forecast of rainfall pattern, and specially ISMR. It was in this background that a programme was initiated at C-MMACS to explore and develop, especially taking advantage of mathematical modelling techniques and high-speed computing, methodologies for long-range forecasting of rainfall patterns. Also, it was felt that one should adopt a composite forecast system, where diverse methodologies could be combined in an internally consistent manner to improve the scope, range and the quality of the forecasts. Accordingly, a three-pronged approach was initiated at C-MMACS combining dynamical forecasting, neural network forecasting and analysis of observed data. Each of these approaches has been developed parallelly, and is briefly described below.

1.1.1 Neural-Network Forecast Model (Cognitive Forecast of Rainfall)

The generalized neural network, designed and developed at C-MMACS termed cognitive network, has been used to generate long-range (one year or more) forecast of ISMR on an experimental basis since 1996. These forecasts, generated well ahead of the particular season, have shown considerable skill over the past few years. In particular, the ISMR for the year 2000 has been forecast as 789 mm, with an error bar of 30 mm. This year, the scope of the forecasts was enhanced to include forecasts of all-India monthly rainfall (AIMR). Since these forecasts have much larger range (several past experimental forecasts, including the forecast for 2000, were generated two years in advance), they can complement and supplement shorter range operational forecasts.

(P. Goswami)

1.1.2 Dynamical Forecast Model (C-MMACS Atmospheric Model)

A fundamental question in dynamical modelling of rainfall seems to be regarding the essential physics that controls this complex process; the relative roles of the host of processes that is likely to be involved are far from clear. Using a novel dynamical scenario, it was possible to show that a very significant part of the observed tropical precipitation can be realized as arising from internal dynamics, essentially an interaction between large-scale circulation and convection. This has evolved into a dynamical forecast model, and the details of the model, its validation as well as forecasts for the weekly progress of summer monsoon of year 2000 have been generated and are available at the C-MMACS web site (www.cmmacs.ernet.in/CAFS).

The dynamical model uses a scenario in which the tropical circulation is visualized as a two-component system: a convective component governed by internal dynamics and a flow governed by slowly varying and stationary forcings: $\zeta_{Total} = \zeta_s + \delta\zeta_c$. ζ represents a dynamical or thermodynamical variable and the subscripts *'s'* and *'c'* refer to the slow and the convective components, respectively; the expansion parameter, δ, takes a value less than unity. It is important to emphasize that the above procedure represents a dynamical partitioning of the tropical circulation. The significance of a dynamical partitioning is that, unlike in a statistical averaging, each dynamically partitioned component has an associated non-negative precipitation *(P)*. One may be tempted to term P_c as 'anomaly' precipitation; this is fine so long as it is not confused with the anomaly precipitation that results from a post-processing (statistical averaging) of observed or simulated data. The convective component is described by the horizontal dynamics of the first baroclinic mode on an equatorial beta-plane, and driven by moist feedbacks.

The slow component is assumed to be such that the associated precipitation is zero. This implies that the

dynamics of the slow component has the value of the associated moisture always close to or less than its equilibrium value. In this approximation, the tropical precipitation is primarily determined by the convective component. However, ζ_s contributes indirectly to the precipitative process through its modulation of the convective component. The specification of the slow component, strictly speaking, should be done either through a model or from observation, with the above constraint. Instead, we shall assume that climatological monthly mean fields provide a reasonable representation of the slow component. Accordingly, we have adopted the 38-year climatology of the low-level monthly mean fields of zonal and meridional winds, derived from Comprehensive Ocean Atmosphere Data Set (COADS) of National Oceanic and Atmospheric Administration (NOAA), USA to represent the slow components. Further, to bring out the features and the variabilities brought about by internal dynamics alone, we consider only climatological annual cycles (CAC) of SST and zonal and meridional winds.

In accordance with our objective, we have generated, for each of the years 1979-88, different model simulations. The initial conditions for each simu–lation were given to be the monthly anomaly (with respect to 38-year CAC) fields from COADS. Since these (statistical) anomaly fields do not necessarily represent the (dynamical) convective components, a one month spin-up time was allowed in each simulation. In each case, simulations were generat–ed for two initial conditions: preceding December and May. An ensemble climatology of the simulations was then generated by composing the two simulations with equal weight. For validation and evaluation of the results, we have considered the Xie-Arkin (XA) monthly precipitation data for the period 1979-1988.

The spatial distribution of correlation coefficients between the observed and the simulated precipitations (corresponding to the December initial condition) for the 120 months of the ten-year period is shown in Fig. 1.1.2.1. The lightest areas are where correlation is above 95% confidence level; the high correlation over parts of the monsoon region is easily seen. Figure 1.1.2.2 compares the time series of normalized (with respect to 120-months mean), area averaged, monthly precipitation over three regions, as indicated. The coefficient of correlation between observation and simulation (*CR*), the ratio of simulated to observed mean (M_R) and, the ratio of simulated to observed standard deviation (s_R), for the area averaged rainfall for the 120 months, are shown in the respective panels. In each of the three regions, the CR is significant at 99% confidence level. However, while the simulated mean and the standard deviation over Region I are very close to the observed values, they are much smaller than the corresponding observed values over Region II and Region III. This, once again, points to the relative role of convective dynamics in determining the precipitation pattern over different regions. While we do have effects of CACs of SST and the low-level winds in the model, the close agreement between the simulated and the observed annual cycles of precipitation is quite striking.

Finally, for future evaluation, we record here the forecasts,

Fig. 1.1.2.1. Longitude-latitude structure of correlation coefficient of observed and simulated monthly precipitation for 120 months. The lightest areas correspond to correlation above 95% confidence level.

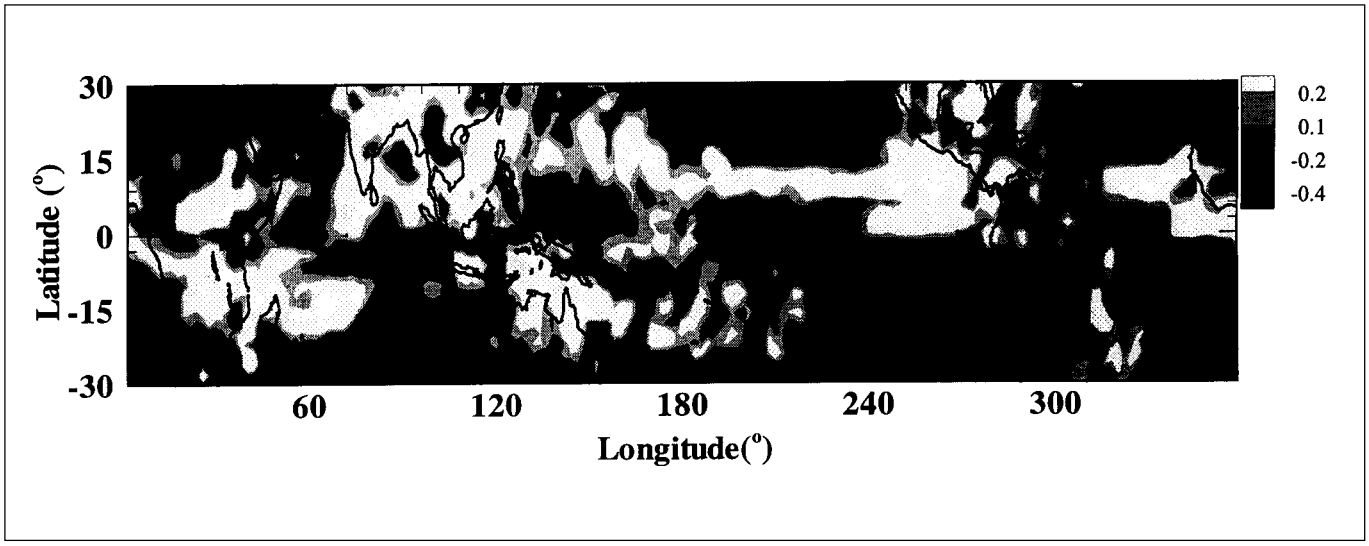

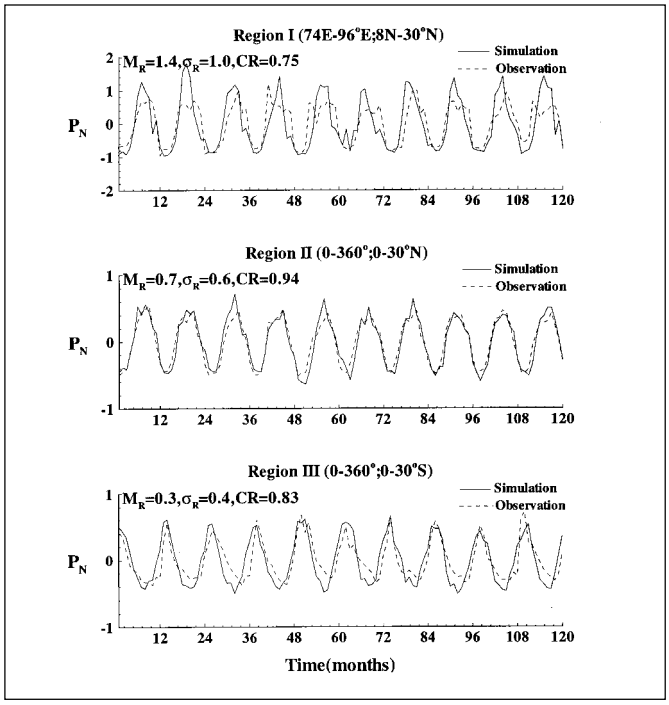

Fig. 1.1.2.2. Comparison of observed (dash lines) and corresponding simulated (solid lines) normalized, area averaged, monthly precipitation for 120 months over three tropical regions as indicated.

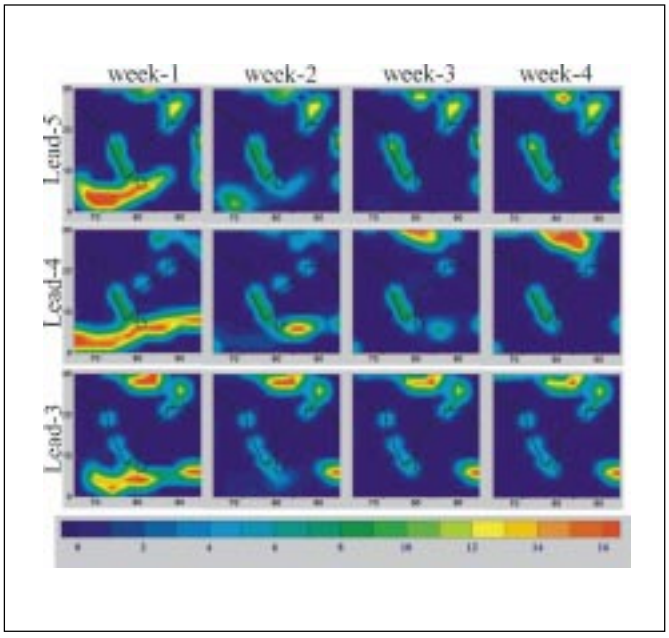

Fig. 1.1.2.3. Experimental forecast of weekly rainfall (mm/day) during the months of (a) June, (b) July, (c) August and (d) September, 2000. The leads 5, 4, 3 refer to the January, February and March initial conditions respectively, calculated from NCEP Reanalysis.

for weekly rainfall, for the months of June to September, 2000 in Fig. 1.1.2.3. These forecasts have been generated using initial conditions derived from National Centre for Environmental Prediction (NCEP) *Reanalyses* for the month of March, 2000; these forecasts are therefore with a lead of 3, 4, 5, and 6 months, for June to September, respectively.

(P. Goswami and K. Rameshan)

1.1.3 Data-based Forecast Model: Index of ISO Activity

Availability of quality and long-period data sets with high frequency, like those available from NCEP and National Centre for Atmospheric Research (NCAR) Reanalyses, for the past forty years, offers excellent opportunities for exploring relationships between variabilities of large-scale systems like monsoons and high-frequency dynamics like intra-seasonal oscillations (ISO). The existence of quasi-periodic oscillations in the Indian summer monsoon (ISM) region has been known for quite sometime. The two most prominent bands in the spectrum of ISO are the 10-20 day quasi-biweekly oscillation (QBW) and a 30-50 day oscillation.

While most studies have focussed on the 30-50 day oscillation, a clear signal at 10-20 day range in the monsoon region has also been reported. Several recent studies demonstrate the dynamical role of QBW oscillation in the circulation in the East Asian summer monsoon (ASM). This close dynamical association between ISO, convective activity and large scale circulation suggests the possibility that ISO activity may play a significant role in the performance of summer monsoon. A conceptual dynamical scenario can be conceived where the intensity and distribution of ISO activity exerts significant control on the performance of the monsoon. The distribution and intensity of the convection centres associated with the convergence/divergence fields of ISO can exert substantial control of rainfall. Indeed, it is conceivable that pre-monsoon ISO activity determines the spatial distribution and strength of the convergence and precipitation centers which, in turn, affects the development of the monsoon heat source. The present work explores such a scenario using NCEP/NCAR Reanalyses data sets.

We have used daily averaged data from the NCEP/NCAR Reanalyses for the period 1958-1997, available on a Gaussian grid. The variables used in this study are, primarily, surface (10 m height) winds and total cloud cover.

To associate the ISO activity with ISM region, the data have been categorized (Table 1.1.3.1) as normal, deficit

and excess years (in comparison to the ISMR) for the corresponding years as follows.

$$R_n(i) = \frac{R(i) - \overline{R}}{\sigma(m)}, \quad i = 1,2, \ldots, 40 \qquad (1)$$

$-0.2 \leq R_n \leq 0.2$ *Normal*

$R_n > 0.2$ *Excess*

$R_n < -0.2$ *Deficient*

where $R(i)$ is the value of ISMR for i^{th} year; $\overline{R}$ and $\sigma(m)$ are the mean and standard deviation of ISMR over a 127 year (1871-1997) period.

To quantify the ISO activity, we have defined an index of ISO activity (IISOA), derived from the power spectrum analysis of the observed data, at a number of locations. We have analysed the power spectrum of the variable at each location for periods upto 100 days. The significant power at a frequency ν, at the location (i,j), and for the n^{th} year n was then defined as

$$\Gamma_\nu(i, j, n) = \begin{cases} P_\nu(i, j, n) - \gamma_\nu(i, j, n) & \text{if } P_\nu > \gamma_\nu \\ 0 & \text{otherwise} \end{cases} \qquad (2)$$

where $\gamma_\nu(i, j, n)$ is the corresponding red noise and P_ν is the corresponding power spectra. By averaging $\Gamma_\nu(i, j, n)$ seperately over normal, excess and deficient years, climatologies were then created for normal years ($\overline{\Gamma}_{N\nu}$), excess years ($\overline{\Gamma}_{E\nu}$) and deficit years ($\overline{\Gamma}_{D\nu}$). It is worth emphasizing that we are looking at *climatology of power spectra and not at power spectra of climatological field.* The normalized anomaly in ISO activity for deficient and excess years at frequency ν and location (i,j) is then defined as

$$\Gamma_{DN}(i, j, \nu) = \frac{\overline{\Gamma}_{D\nu}(i, j) - \overline{\Gamma}_{N\nu}(i, j)}{\overline{\Gamma}_{N\nu}(i, j)} \qquad (3)$$

$$\Gamma_{EN}(i, j, \nu) = \frac{\overline{\Gamma}_{E\nu}(i, j) - \overline{\Gamma}_{N\nu}(i, j)}{\overline{\Gamma}_{N\nu}(i, j)} \qquad (4)$$

To examine the association between ISO activity and ISM, different latitudes such as 10 °S, equator, 10 °N and 20 °N are considered to cover the equatorial belt over which Tropical Convergence Zone (TCZ) is active. With those latitudinal points, twenty locations (30 °E to 125 °E, at intervals of 5 degrees) were chosen, covering the ISM region in the zonal direction. These locations were chosen so as to cover the areas over which significant ISO activities are seen. The power spectra were calculated using the PSD module of MATLAB library, with a Butterworth filter. The variables considered in the present study are the surface wind field and the total cloud amount.

Table 1.1.3.1. Index of ISO activity at 20 °N and over four longitudinal positions for 28 normal, excess and deficit monsoon years.

Year*	R_n	category	η at 20° N				
			85° E	90° E	95° E	100° E	ϕ
1959	1.0	Exess	-0.36	-0.37	-0.39	-0.30	-1
1961	2.0	Exess	0.04	0.32	0.11	-0.20	1
1962	-0.5	Normal	1.05	1.16	0.93	1.01	-1
1964	0.8	Exess	-0.09	-0.07	-0.24	-0.17	-1
1965	-1.7	Deficit	-0.01	0.12	-0.01	0.26	-1
1966	-1.4	Deficit	-0.05	0.02	-0.12	0.42	1
1968	-1.1	Deficit	-0.35	-0.28	-0.27	0.09	1
1970	1.1	Exess	-0.06	0.16	0.05	0.12	1
1971	0.4	Normal	-0.10	0.27	0.59	0.02	1
1972	-2.3	Deficit	-0.14	-0.28	-0.16	-0.05	1
1973	0.7	Normal	0.89	0.22	0.21	0.35	1
1974	-1.2	Deficit	0.04	-0.24	-0.06	-0.21	1
1975	1.3	Exess	-0.11	-0.21	-0.27	0.12	-1
1979	-1.7	Deficit	-0.11	-0.12	-0.07	-0.02	1
1980	0.4	Normal	0.26	-0.29	0.31	0.10	1
1982	-1.4	Deficit	0.38	0.56	0.14	0.75	-1
1983	1.2	Exess	-0.16	-0.10	0.26	0.44	1
1985	-0.7	Normal	0.04	-0.04	0.35	0.53	-1
1986	-1.2	Deficit	0.86	0.12	1.28	0.38	-1
1987	-1.9	Deficit	-0.17	0.61	-0.10	0.26	-1
1988	1.7	Exess	0.86	-0.04	0.04	0.16	1
1990	0.8	Normal	-0.21	0.44	0.95	0.19	1
1991	-0.8	Normal	-0.29	0.67	0.39	0.67	-1
1992	-0.8	Normal	0.01	0.09	0.70	0.24	-1
1993	0.6	Normal	0.65	0.46	1.47	0.42	1
1994	1.0	Exess	0.24	0.77	0.41	0.16	1
1995	0.5	Normal	1.12	-0.09	0.03	-0.07	1
1996	0.6	Deficit	1.29	0.19	0.03	1.03	1
Sucess			54%	43%	68%	50%	

* The years between 1958 to 1997 that do not appear are normal monsoon years.

Figure 1.1.3.1 shows power spectra averaged over the normal years (Fig. 1.1.3.1 (a)), excess years (Fig. 1.1.3.1 (b)) and deficit years (Fig. 1.1.3.1 (c)) for the ISO range in the surface zonal wind from NCEP Reanalyses; the dashed line in each panel represents the corresponding red noise level. As can be seen from these figures, the ISO signal is also a strong function of location. A comparison of Figs. 1.1.3.1 a-c, also shows considerable variation in the characteristics of the power spectra for the normal, excess and deficit years, thus providing a confirmation of our informed guesses. However, Fig. 1.1.3.1 shows that the maximum difference among normal, excess and deficit

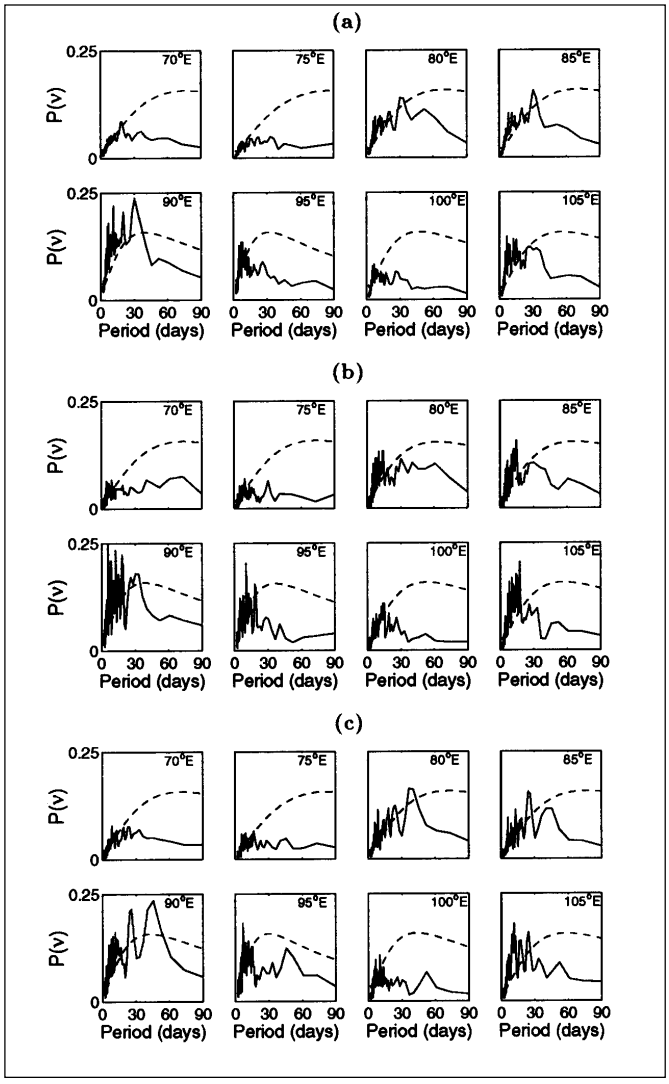

Fig. 1.1.3.1. Averaged power spectra for surface zonal wind over 20 °N for, (a) normal years, (b) excess years and (c) deficit years. The dashed line in each pannel represents the corresponding red noise level.

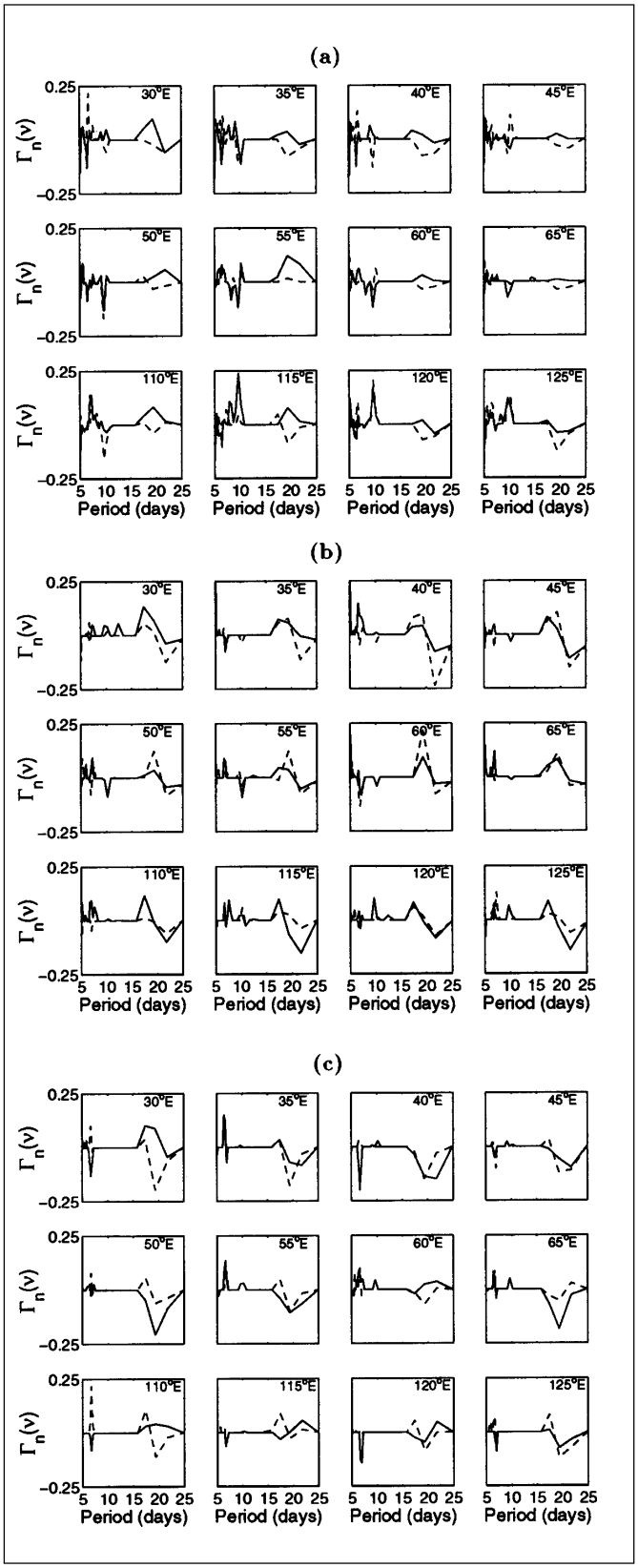

Fig. 1.1.3.2. Normalized difference in power spectra for excess years (solid lines) and deficit years (dashed lines), of surface wind field, for the entire year at, (a) 20 °N, (b)10 °N and, (c) Equator: twelve longitudinal locations are considerd , divided west and east of the summer monsoon region.

years lies in the frequency range of 10-20 days. In the subsequent analysis, therefore, we shall consider the frequency range 5-25 days to investigate further the differences among normal, excess and deficit years. Fig. 1.1.3.2 shows the behaviour of $\Gamma_{EN}(i, j, v)$ (solid lines) and $\Gamma_{DN}(i, j, v)$ (dashed lines) over twelve longitudes at each of three latitudes. A clear distinction between the excess years and the deficit years is visible in quite a few cases.

In Figs. 1.1.3.1 and 1.1.3.2, the power spectra were calculated using daily data for the entire year. For operational applications, however, it will be useful only if such a signal is present over the pre-monsoon period. A question which is important, both for conceptual understanding and practical application, is whether any association of monsoon performance exists with ISO activity in the premonsoon period. Existence of such an

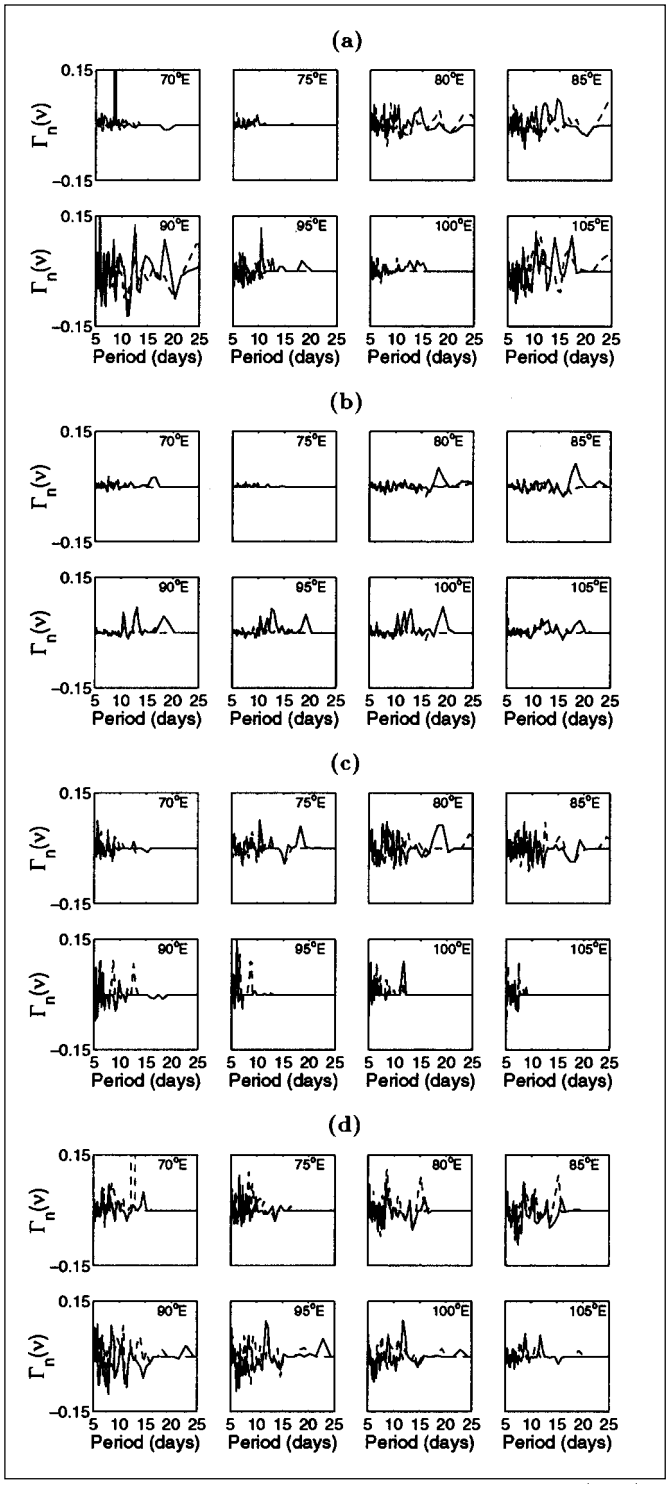

Fig. 1.1.3.3. Normalized difference in power spectra for excess years (solid lines) and deficit years (dashed lines), of total cloud amout, for the pre-monsoon period Dec-May at, (a)20 °N, (b)10 °N, (c) Equator and (d) 10 °S.

association would imply that the pre-monsoon ISO activity could be used to predict overall monsoon performance in the subsequent season. Conceptually, such as association would indicate that distribution of pre-monsoon convective activity has appreciable influence over monsoon. To examine the above question, we have examined ISO activity over two pre-monsoon periods, December-May and Jan-Jun and, also, from October of the preceding year to April of the considered year. For operational applications, it is important to examine whether the signal also exists in other variables, especially in variables more easily obtainable through satellite observations. The normalised difference in power spectra of the cloud amount for the pre-monsoon period (Dec-May) is depicted in Fig. 1.1.3.3. Eight longitudinal locations are considered (70 °E to 105 °E, with 5 degrees interval). It can be seen that the clearest distinction between the excess and deficit years over 10 °N latitude between 90 °E to 105 °E is around the 20 days period. To assess the success of the method in estimating the Inter Annual Variability (IAV) of summer monsoon, an IISOA integrated over the frequency range of 16-19 days was defined as follows.

$$\eta(i,j,n) = \sum_{k=1}^{4} \left[\Gamma(i,j,n,\nu_k) - \overline{\Gamma_\nu}(i,j,\nu_k) \right] \qquad (5)$$

The values of η calculated at 20 °N and, for four longitudes are shown in Table 1.1.3.1 for 28 excess and deficit years. The quantity ϕ, where $\phi = 1(-1)$ if the sum of the four values of η have the same (opposite) sign as the departure from normalised rainfall, measures how often the IISOA captures the trend of ISMR. In the present case, $\phi = 1$ in 18 out of 28 cases, implying a success rate of about 68%.

The present study thus indicates that ISO activity can be a potential predictor for summer monsoon performance. This also highlights the importance of identification of appropriate signals for greater predictability. While a clearer understanding of dynamical mechanisms behind such an association is necessary for assessing its implications on predictability, immediate use of ISO activity for forecast of monsoon performance is possible through use of data generated from various field experiments.

(P. Goswami, P. V. S. Raju and U. C. Mohanty**)*
*(*CAS, **IIT, Delhi)*

A composite forecast, then, would utilise all the three subsystems, checking internal consistency wherever applicable, to generate a comprehensive and more reliable forecast. *(P. Goswami)*

1.2 Ocean Modelling Activities

1.2.1 Thermal Structure

The 3-D thermal structure in Modular Ocean Model (MOM) is determined by the heat flux input on the surface and the

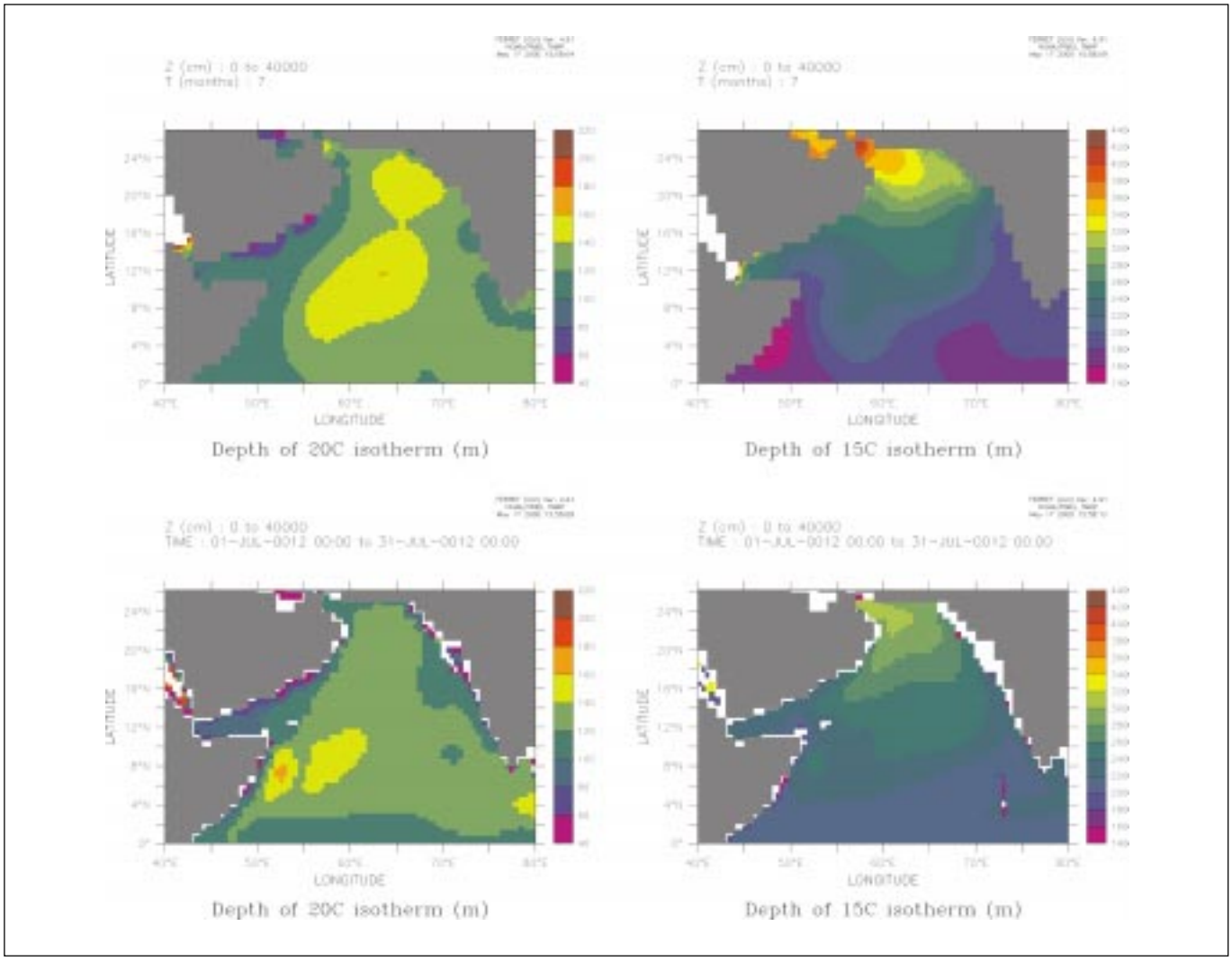

Fig. 1.2.1.1. Comparison between Levitus climatology (top panels) and MOM simulations (bottom panels) for the locations of 20 ºC and 15 ºC isotherms in July.

mixing in the model. In our earlier runs of MOM, we used a purely restoring kind of flux condition at the top where the sea surface temperature (SST) was damped to climatological SST with a time constant. However, this resulted in very shallow mixed layer at several places because the entire restoring flux was added to the top grid box. Because our vertical resolution is 10 m near the surface, we felt that the shortwave flux must be prescribed and allowed to penetrate into the deeper levels in order to avoid shallow mixed layers.

There is considerable uncertainty in the specification of heat and salt fluxes as they are determined as a sum of sensible heat, latent heat, solar and longwave radiation fluxes, precipitation and evaporation, each with its own margins of error. Atlases compiled by different researchers show wide variation amongst them. In addition, most of the atlases are compiled by objective analysis based on the prescription that the net flux over the whole globe in a year should be zero. While these fluxes work well in global models, where such a condition is implicit, they do not apply to regional models. Based on actual measurements reported in the Arabian Sea over the past few years, we have used a combination of fluxes from several sources. However, the net flux over the whole domain, over the whole year, is non-zero and this would introduce drifts in the model. In order to reduce this drift, a new module which combines the actual flux with a Newtonian damping term where the surface SST's are damped back to climatology was developed and implemented.

With regard to mixing, we employ a Richardson number-based scheme for vertical mixing and a Laplacian scheme for the horizontal. Although this was shown to work quite well in the tropics, advanced schemes such as isopycnal mixing must be incorporated for better

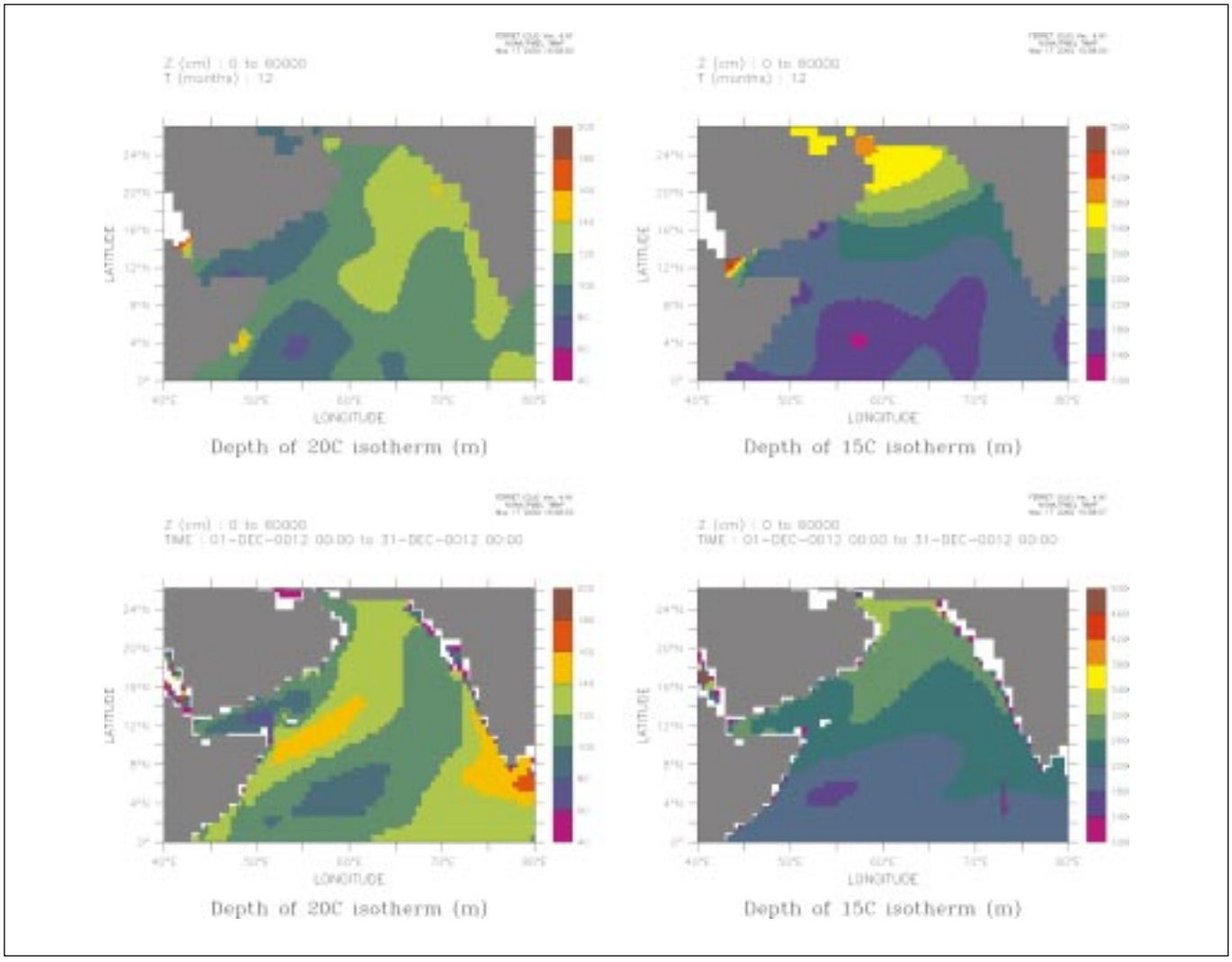

Fig. 1.2.1.2. Comparison between Levitus climatology (top panels) and MOM simulations (bottom panels) for the locations of 20 °C and 15 °C isotherms in December

simulations. However, want of computing resources has delayed the implementation of such schemes and we hope to try out them fairly soon.

In order to resolve the vertical structure better, we refined the model to have 35 levels in the vertical (10 in the top 100 m and other levels to closely match Levitus standard depths). The horizontal resolution was 0.4 degrees east-west and varying resolution north-south (from 1 degree at 15 °S to 0.4 degree at 25 °N). Sponge boundaries were applied at 15 °S and the eastern end was closed allowing no interaction with the Pacific.

The results of the simulation in the twelfth year of integration from rest using climatological forcing along with Levitus climatological fields for the Arabian Sea are shown in Figs 1.2.1.1 and 1.2.1.2, which correspond to the months of July and December, respectively. In both the figures, the depth of 20 °C isotherm (left panels) and 15 °C isotherm (right panels) are extracted from the 4-D fields and contoured. The top panels are from Levitus climatology while the bottom ones are model results averaged over a month. The agreement between the two at 20 °C depth in July is remarkably good (within 20 m of each other), except for larger differences near the Somali region. At the 15 °C isotherm level, the differences are larger (40 m or so) but comparable to model resolution at these depths. In December, the agreement between the two is still quite good, except, again, for the Somali region, and the southern tip of India.

(P. S. Swathi and C. Kalyani Devasena)

1.2.2 Runs with Satellite Winds

One of the goals of the Indian Ocean Model and Dynamics (INDOMOD) project is the development of an experimental

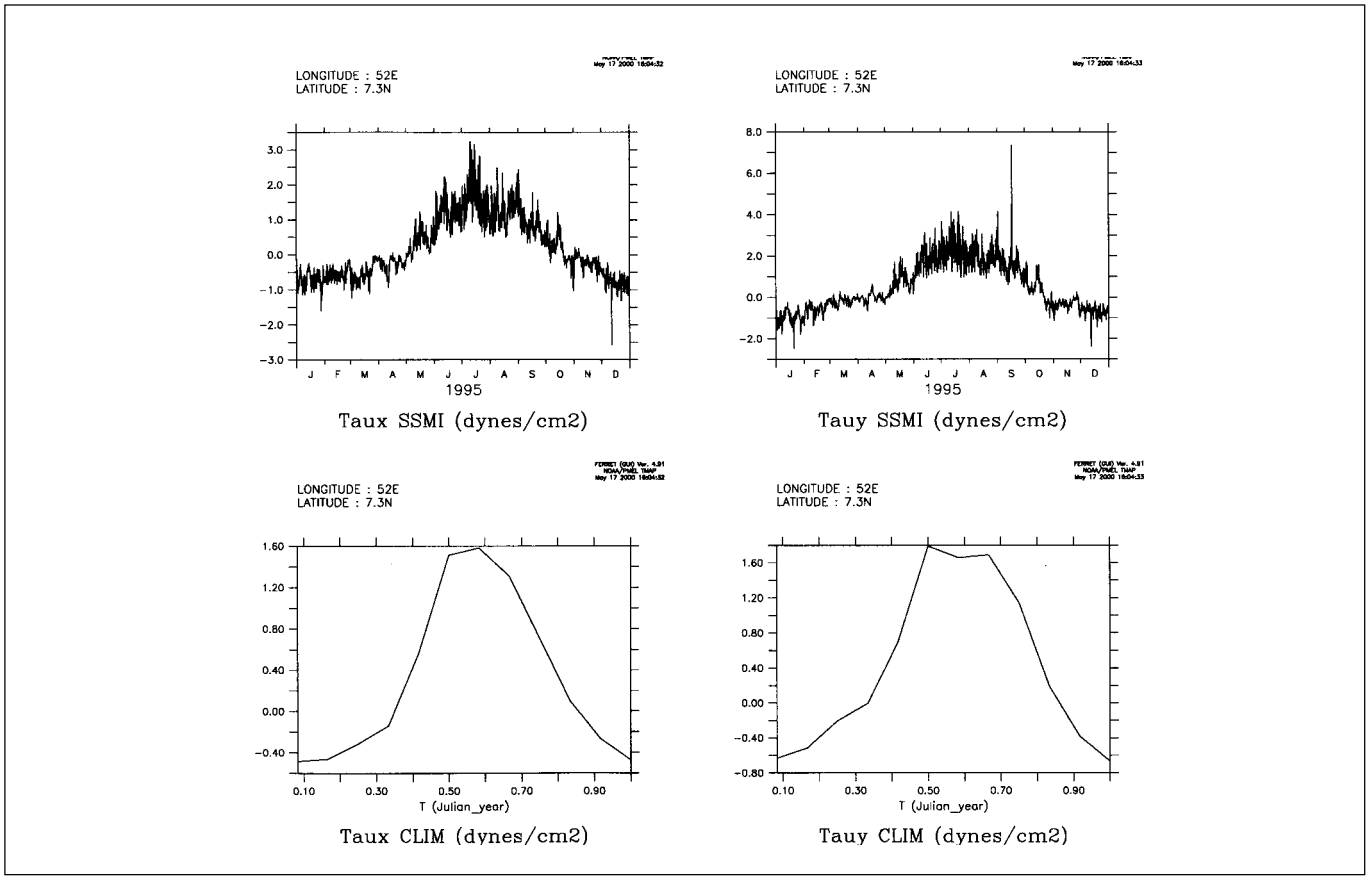

Fig. 1.2.2.1. Six-hourly wind stresses from SSMI (top panels) and monthly-mean climatology (bottom panels) at (52 °E,7.3 °N).

forecasting system for shorter temporal scales. In order to test the variability of the model at shorter time scales, we forced the model with 6-hourly Special Sensor Microwave Imager (SSMI) derived winds for the years 1994-1996. The winds were first checked against monthly climatologies by averaging them over a month and found to be acceptable. However, the high frequency variability in the SSMI winds introduces major changes to the circulation in the Indian Ocean. As an example, the variability of SSMI windstresses (top panels) at a point (52 °E, 7.3 °N) during 1995 and the climatology (bottom panels) are shown in Fig. 1.2.2.1. Notice the high frequency variability in satellite winds. Such a variability exists throughout the Indian Ocean basin.

The effect of this high frequency variability on the circulation is dramatic. The average kinetic energy (KE) (left panels) and average variance in temperature (right panels) over the whole domain for SSMI (top panels) and climatological (bottom panels) runs are shown in Fig. 1.2.2.2. The KE of the SSMI run is more than double that of the climatological run with pronounced peaks in the beginning of May and in November, which are absent in the climatological run. The variance in the thermal structure is, however, comparable between the two, indicating that the highly variable winds have a stronger effect on the circulation compared to the thermal structure.

We have compared snapshots of the velocity fields (averaged over the top 50 m) between SSMI and climatological runs for two days in July (left panels) and November (right panels) in Fig. 1.2.2.3 for illustrative purposes. Notice the strong intensification of the Somali jet in July with SSMI winds. However, the intensification of the North Equatorial Current (NEC) during November with SSMI winds is dramatic leading to the high KE seen in Fig. 1.2.2.2. A comparison of the wind stresses at this time (not shown) does not indicate such a strong surface forcing and this intensification must be remotely forced.

(P. S. Swathi and C. Kalyani Devasena)

1.2.3 Porting of MOM_3 to Origin 200

V. Balaji of SGI and Geophysical Fluid Dynamics Laboratory (GFDL), USA visited C-MMACS in the first week of January. He is the author of all the parallel code in MOM_3. Utilising his presence, we ported MOM_3 to the Origin 200 using multiple processors for test cases. In

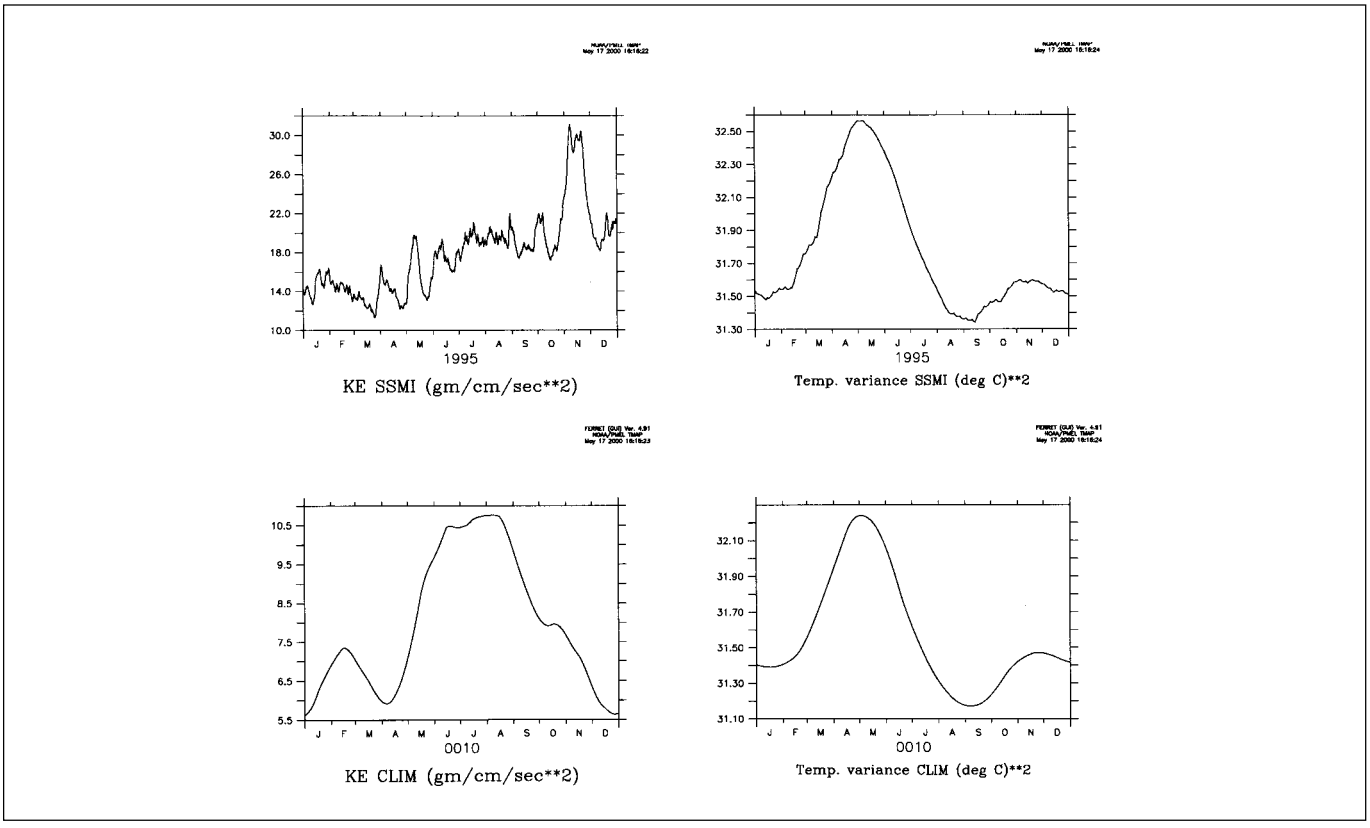

Fig. 1.2.2.2. Average kinetic energy (KE) (left panels) and variance of temperature (right panels) for the SSMI (top panels) and climatology (bottom panels) runs.

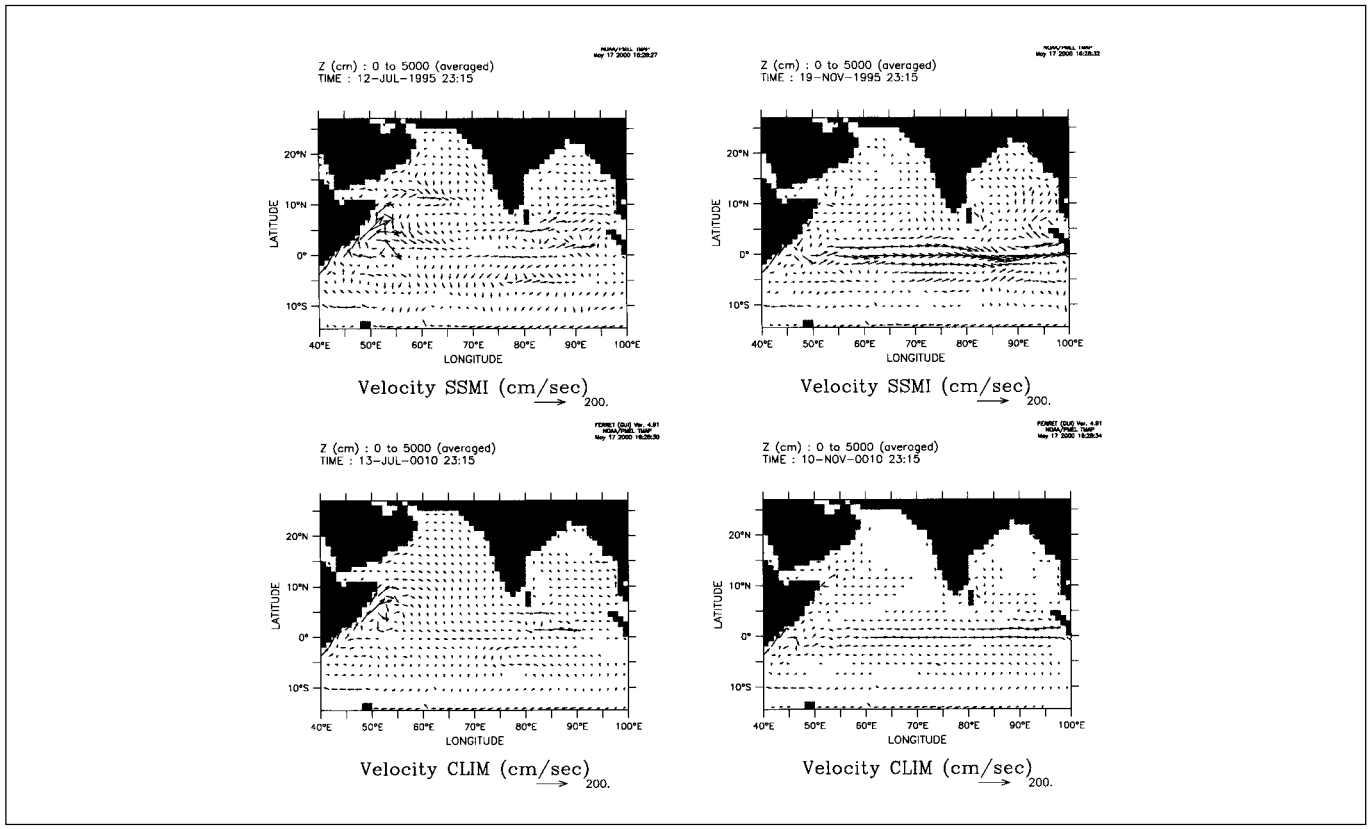

Fig. 1.2.2.3. Snapshots of average velocity in the top 50 m in July (left panels) and November (right panels) for SSMI (top panels) and climatology (bottom panels) runs.

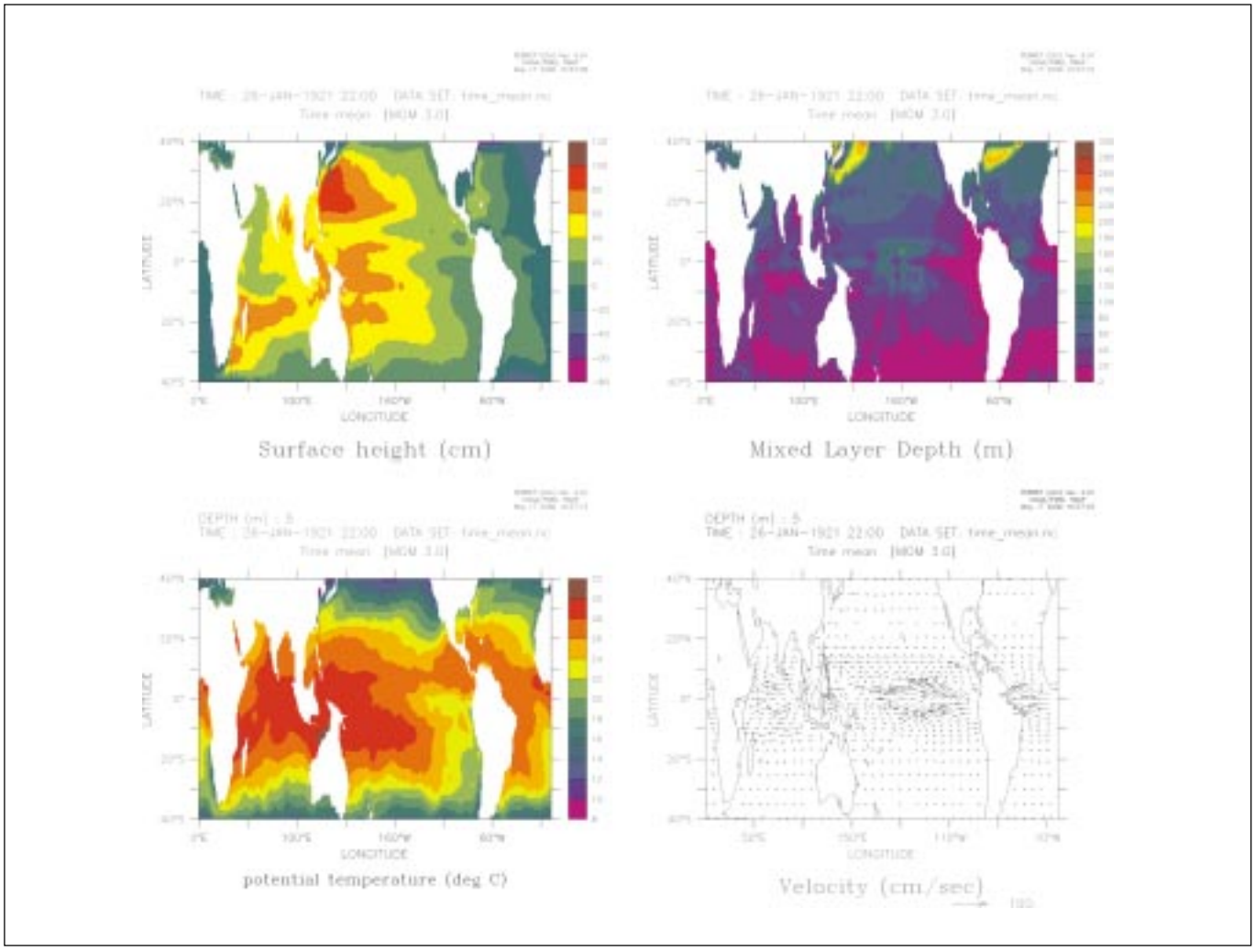

Fig. 1.2.3.1. Monthly-mean fields for January from MOM_3 global simulations; (clockwise from top left) sea surface height, mixed layer depth, surface velocity and temperature.

comparison to MOM_2, MOM_3 is highly versatile with several new modules, especially for mixing, free surface and parallel implementation.

Subsequently, a realistic global run using monthly-mean climatological data sets for forcing and a restart file from an on-going integration at GFDL was set up. The model has 362 x 200 x 40 grid points with 1 degree resolution in the zonal direction and varying resolution in the meridional direction and depth. The run invokes the new k-profile parameterisation (kpp) mixing scheme for vertical mixing, Gent-Mcwilliams scheme for isopycnal diffusion, explicit free surface formulation, quicker scheme for tracer diffusion and partial bottom cells for bottom topography. A one month average of various fields in January are shown in Fig. 1.2.3.1. Comparison of these fields with climatological atlases have shown the simulations to be quite accurate. Further runs with MOM_3 on both regional and global domains will be pursued in the coming year after the acquisition of the new Large Compute Server.

(P. S. Swathi and R. P. Thangavelu)

1.2.4 MSMR Validation

The Satellite Applications Centre (SAC), Ahmedabad convened a meeting of users of the Multispectral Microwave Radiometer (MSMR) payload on the Indian satellite IRS-P4 in March, 2000 as a part of the validation exercise. The satellite was launched in May, 1999 and after initial calibration exercises, a set of sea surface temperature (SST) data for nearly two months was made available to users a few weeks prior to this exercise. As the amount of data was too little to force the ocean model for any useful study, we decided to check the accuracy of the data against data from other potentially more accurate sensors on NOAA satellites. (The sensors on NOAA satellites are based on infrared sensors, the Advanced Very

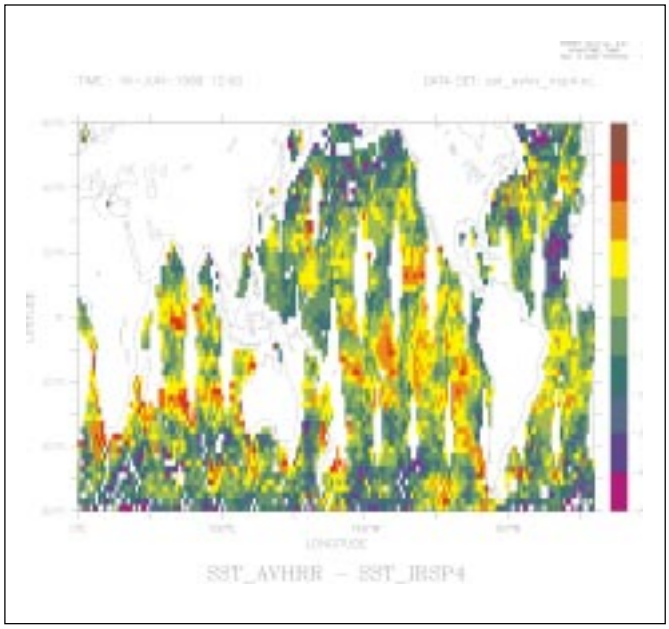

Fig. 1.2.4.1. Differences between AVHRR and MSMR (IRS-P4) sea surface temperatures.

High Resolution Radiometer (AVHRR) and have potentially better spatial resolution and accuracy).

The AVHRR daily composite data for concurrent days was downloaded from NOAA. The data from SAC were from actual passes of the satellite and this was binned on a 1 degree by 1 degree grid. Comparison of the two (Fig. 1.2.4.1) for one day showed good agreement over most of the earth but there were regions where the differences are over 2 °C. A similar comparison on weekly averaged Reynolds SSTs performed by both C-MMACS and SAC showed similar results. The accuracy of MSMR is of the order of 1-2 °C as per instrument calibration and this exercise confirmed the expectations.

(P. S. Swathi and C. Kalyani Devasena)

1.3 Sea Level Variations

Most of the earlier work in published literature concentrate on the application of linear stochastic time series models like ARIMA to tide gauge data for coastal stations in India.

Nonlinear analysis of sea level data using a fractal interpolation technique conducted earlier yielded fractal dimensions between 1.2 and 1.3 for five Indian coastal stations. This analysis, when further extended to four more Indian stations, along with stations in Singapore, Thailand and China, yielded a similar result. The conclusion from these two studies is that sea level variation is a low order dynamical system. A similar procedure applied to a data set of geologic time scales (296-292 My) yielded a fractal dimension of 1.4.

Two of the many techniques for model building for prediction of non-stationary and nonlinear time series are, (a) time dependent auto regressive models and, (b) the construction of dynamical inverses using singular value decomposition. However, neither of these techniques have been applied to analyse sea level variations as yet. We have applied nonlinear techniques such as time-dependent AR models to the data on sea level variations and work is in progress to build up models based on the same.

The solution of the dynamical inverse problem (DIP) (i.e., generating a low order system of ordinary differential equations to capture the variability) has also been taken up. To begin with, numerical experiments were conducted on Lorenz type equations to study the stability of the DIP under different levels of noise. Using this experience, we aim to construct DIP models for sea level variations at each station along the Indian coast.

(N. K. Indira)